

## Feasibility study of endoscopic x-ray luminescence computed tomography: Simulation demonstration and phantom application

Xueli Chen, Jimin Liang, Xin Cao, Defu Yang, Dongmei Chen et al.

Citation: *J. Appl. Phys.* **114**, 084701 (2013); doi: 10.1063/1.4819299

View online: <http://dx.doi.org/10.1063/1.4819299>

View Table of Contents: <http://jap.aip.org/resource/1/JAPIAU/v114/i8>

Published by the AIP Publishing LLC.

---

### Additional information on J. Appl. Phys.

Journal Homepage: <http://jap.aip.org/>

Journal Information: [http://jap.aip.org/about/about\\_the\\_journal](http://jap.aip.org/about/about_the_journal)

Top downloads: [http://jap.aip.org/features/most\\_downloaded](http://jap.aip.org/features/most_downloaded)

Information for Authors: <http://jap.aip.org/authors>

## ADVERTISEMENT



Now Indexed in  
Thomson Reuters  
Databases

Explore AIP's open access journal:

- Rapid publication
- Article-level metrics
- Post-publication rating and commenting

# Feasibility study of endoscopic x-ray luminescence computed tomography: Simulation demonstration and phantom application

Xueli Chen,<sup>1,a)</sup> Jimin Liang,<sup>1</sup> Xin Cao,<sup>1</sup> Defu Yang,<sup>1</sup> Dongmei Chen,<sup>1</sup> Jorge Ripoll,<sup>2</sup> and Jie Tian<sup>1,3,a)</sup>

<sup>1</sup>*School of Life Science and Technology, Xidian University, Xi'an 710071, China*

<sup>2</sup>*Department of Biomedical and Aerospace Engineering, Universidad Carlos III de Madrid, 28911 Leganes, Madrid, Spain*

<sup>3</sup>*Institute of Automation, Chinese Academy of Sciences, Beijing 100190, China*

(Received 25 June 2013; accepted 7 August 2013; published online 27 August 2013)

Even though endoscopic fluorescence diffuse optical tomography (eFDOT) exhibits significant potential, currently its application is limited due to the existence of strong autofluorescence and the imaging inaccuracy caused by a very short source-detector distance. Motivated by the emerging X-ray luminescence computed tomography (XLCT) technology, we presented an endoscopic XLCT (eXLCT) methodology. In the methodology, the aperture angle of the objective was incorporated into the forward model, providing a more accurate description of light propagation. Numerical simulation with a heterogeneous geometry and an imaging experiment with a physical phantom were illustrated to demonstrate the feasibility of the presented eXLCT methodology.

© 2013 AIP Publishing LLC. [<http://dx.doi.org/10.1063/1.4819299>]

## I. INTRODUCTION

Fluorescence diffuse optical tomography (FDOT), as a promising molecular imaging technique, has been widely applied to small-animal or superficial organ imaging, in which the imaging object can be measured or transilluminated externally.<sup>1–3</sup> Its endoscopic counterpart, endoscopic fluorescence diffuse optical tomography (eFDOT), has also been developed for imaging the internal organs that are deep inside a large animal or human body by taking source-detector fibers close to the region of interest in a minimally invasive manner through the saccular or tubular organs.<sup>4,5</sup> However, two drawbacks limit its immediate translation to wide applications. First, the existence of autofluorescence induced by the external near-infrared (NIR) light excitation degrades the quality of reconstructed images, a problem also inherent in FDOT.<sup>6</sup> Second, the source-detector fibers are circularly distributed at the head of endoscopic probe with a hollow annular shape. This leads to several source-detector pairs being an very short distances apart, with inaccurate modeling and loss of information as a consequence.<sup>4</sup>

One of the available approaches to overcome this problem is to use an external excitation while carrying out detection using an endoscopic probe. However, fluorescent probes are embedded in a highly scattering and absorbing medium, so that probes might receive very little excitation light through external transillumination. Recently, an emerging molecular imaging modality termed X-ray luminescence computed tomography (XLCT) has been presented as a means of imaging small-animal-sized objects.<sup>7,8</sup> Utilizing the characteristics of phosphor nanoparticles being stimulated by X-rays to emit NIR light, XLCT employs an X-ray beam as the excitation light and uses a charge coupled device (CCD) camera to measure the emitted NIR light.<sup>7,8</sup> Using

the X-ray excitation, XLCT does not suffer from the autofluorescence contribution and bears a localized and deep probing capability.<sup>8</sup> Motivated by the advantages of XLCT and endoscopic imaging technology, we imagine whether the endoscopic acquisition mode can be integrated into the XLCT technology to figure out the awkwardness that the eFDOT faced currently.

In this paper, we first presented an endoscopic XLCT (eXLCT) methodology which overcomes the current drawbacks of eFDOT and then theoretically demonstrated its feasibility. By selecting cone-beam X-rays as an external excitation source and using an endoscopic detector to collect the emitted NIR light, additionally eliminating the drawbacks of eFDOT, eXLCT provides an accurate image of an internal organ inside a large body instantaneously. The purpose of using the cone-beam X-rays is to obtain the anatomical structure of samples, providing a priori information. In the methodology, the aperture angle of the objective was incorporated into the forward model, providing a more accurate description of light propagation. In the following, we first report the theoretical basis for the proposed eXLCT setup, including both the construction of an accurate forward model and the development of an effective reconstruction algorithm and then demonstrate its effectiveness by performing a numerical simulation in a tissue-mimicking medium and an imaging experiment in a physical phantom.

## II. METHODOLOGIES

### A. Forward model: Hybrid light transport model

Figure 1 illustrates the representative tomographic setups mentioned in this paper, where Fig. 1(a) is the setup for the traditional FDOT, Fig. 1(b) for the eFDOT, Fig. 1(c) for the existing XLCT, and Fig. 1(d) for the proposed eXLCT. In Fig. 1(d),  $\Omega_{dt}$  denotes the region of the scattering tissues,  $\Omega_{oc}$  shows the region of the organ cavity, and  $B$  specifies the

<sup>a)</sup>Electronic addresses: xlchen@xidian.edu.cn and tian@ieee.org.

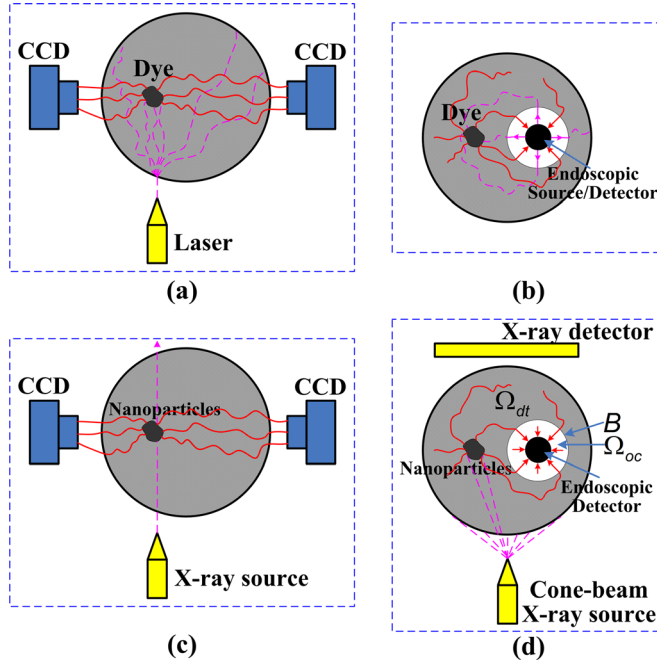


FIG. 1. Representative tomographic setups. (a) Traditional FDOT, (b) eFDOT, (c) XLCT, and (d) proposed eXLCT.

interface between  $\Omega_{dt}$  and  $\Omega_{oc}$ . In the proposed eXLCT setup, the cone-beam X-ray tube and flat panel detector are used to obtain the structure of the sample and to provide the location of the endoscopic detector. To reconstruct the distribution of phosphor nanoparticles, we should first develop a forward model which accounts for the propagation of both the X-rays and NIR light.

Due to the high-energy characteristics of X-rays, it is often assumed that an X-ray beam is limited to its primary path and propagates through biological objects along a straight line. Thus, the X-ray intensity distribution along the primary path is determined by<sup>8</sup>

$$I(r) = I_0(r_0) \exp\left(-\int_0^1 \mu_t((1-\tau)r_0 + \tau r) d\tau\right), \quad (1)$$

where  $r_0$  is the irradiating position of the X-ray beam on the body surface,  $I_0$  is the X-ray intensity at  $r_0$ ,  $\mu_t$  is the attenuation coefficient of the X-ray beam in a biological object,  $r$  is a position in the biological object, and  $I(r)$  denotes the X-ray intensity at  $r$ .

When an X-ray beam travels some distance in a biological object and encounters phosphor nanoparticles, these nanoparticles will be excited to emit NIR light. To accurately localize and reliably quantify the distribution of phosphor nanoparticles in the object, the propagation of the emitted NIR light in the endoscopic geometry shown in Fig. 1(d) should be modeled. In the endoscopic geometry, the NIR light emitted from the phosphor nanoparticles first propagates in the scattering regions to reach the interface  $B$  and then goes across a nonscattering region formed by the organ cavity before being detected by the endoscopic detector. Thus, the NIR light propagation model must possess the ability of describing the light propagation in both scattering

and nonscattering regions. In the scattering region, the diffusion equation and related boundary condition are used to describe the NIR light propagation:

$$\begin{aligned} -\nabla \cdot (D(r)\nabla\phi(r)) + \mu_a(r)\phi(r) &= S(r), \quad r \in \Omega_{dt}, \\ \phi(r) + \alpha(r)D(r)(v(r) \cdot \nabla\phi(r)) &= 0, \quad r \in \partial\Omega_{dt}, \end{aligned} \quad (2)$$

where  $\partial\Omega_{dt}$  is the boundary of the scattering region and satisfies  $\partial\Omega_{dt} \supset B$ ,  $\phi(r)$  is the nodal flux density,  $D(r)$  is the diffusion coefficient,  $\mu_a(r)$  is the absorption coefficient,  $\alpha(r)$  is the mismatch factor of the refractive index,  $v(r)$  is the outward unit normal vector on the boundary  $\partial\Omega_{dt}$ , and  $S(r)$  denotes the power density of the emitted NIR light. Because the power density of the emitted NIR light is linearly proportional to both the X-ray dose and the distribution of the phosphor nanoparticles, the following formula for the power density of the emitted NIR light is obtained:

$$S(r) = \varepsilon I(r) \rho(r) \frac{1}{V(r)}, \quad (3)$$

where  $\varepsilon$  is the NIR quantum yield times the absorption cross section of the phosphor nanoparticles at X-ray energies,  $\rho(r)$  represents the concentration of the phosphor nanoparticles, and  $V(r)$  is the volume of the phosphor nanoparticles.

When the NIR light reaches the interface  $B$  and propagates into the nonscattering region, diffuse NIR light transforms into nondiffuse light. Thus, the following refractive-index-mismatched boundary condition was constructed to describe the transformation:

$$J(r') = \frac{1}{\alpha(r')} \phi(r'), \quad (4)$$

where  $r'$  is a point on the interface  $B$ ,  $J(r')$  is the light flux rate toward the inside of the nonscattering region, and  $\phi(r')$  is the light flux constructed by the NIR light propagating in the scattering region.

Similar to light propagation in free space,<sup>9</sup> the NIR light propagation from the interface  $B$  to the endoscopic detector was characterized by the following equation:

$$\begin{aligned} P(r_d) &= \int_B J(r') \xi(r', r_d) \frac{\cos\theta_{r'} \cos\theta_{r_d}}{|r_d - r'|^2} \\ &\times \exp(-\mu'_a |r_d - r'|) dB, \quad r' \in B, r_d \in R, \end{aligned} \quad (5)$$

where  $R$  denotes a space constructed by the endoscopic detector,  $r_d$  is a detection point at  $R$ ,  $P(r_d)$  is the corresponding light power,  $\theta_{r'}$  and  $\theta_{r_d}$  are angles between the surface normal at  $r'$  and  $r_d$ , respectively, with the directional vector from  $r'$  to  $r_d$ ,  $\mu'_a$  is the absorption coefficient of the nonscattering region, and  $\xi(r', r_d)$  denotes a visibility factor. Considering the structure of the detector array commonly used in the eFDOT setup and in the specific medical endoscope, as shown in Fig. 2(a), the visibility factor is defined by incorporating the aperture angle of the objective lens:

$$\xi(r', r_d) = \begin{cases} 1, & \cos^{-1}\left(\frac{r' - r_d}{|r' - r_d|} \cdot n_d\right) \leq \frac{\beta}{2}, \\ 0, & \text{otherwise} \end{cases} \quad (6)$$

where  $\mathbf{n}_d$  is the surface normal of the objective, and  $\beta$  is its aperture angle, as shown in Fig. 2(b).

Based on the aforementioned analysis of both X-ray and NIR light propagation, the forward model of the eXLCT can be obtained as follows by combining Eqs. (1)–(6):

$$\begin{cases} -\nabla \cdot (D(\mathbf{r}) \nabla \phi(\mathbf{r})) + \mu_a(\mathbf{r}) \phi(\mathbf{r}) = \varepsilon I_0(\mathbf{r}_0) \exp\left(-\int_0^1 \mu_t((1-\tau)\mathbf{r}_0 + \tau\mathbf{r}) d\tau\right) \rho(\mathbf{r}) \frac{1}{V(\mathbf{r})}, & \mathbf{r} \in \Omega_{dt} \\ P(\mathbf{r}_d) = \int_B \frac{1}{\alpha(\mathbf{r}')} \phi(\mathbf{r}') \xi(\mathbf{r}', \mathbf{r}_d) \frac{\cos \theta_{r'} \cos \theta_{r_d}}{|\mathbf{r}_d - \mathbf{r}'|^2} \exp(-\mu'_a |\mathbf{r}_d - \mathbf{r}'|) dB, & \mathbf{r}' \in B, \mathbf{r}_d \in R. \end{cases} \quad (7)$$

## B. Inverse reconstruction: Finite element discretization and sparse reconstruction

Using the finite element method, the forward model is converted into a matrix equation that links the distribution of phosphor nanoparticles and the measurements at the endoscopic detector

$$\Sigma [M^{-1}F]_{\phi_B} \rho = P, \quad (8)$$

where  $[M^{-1}F]_{\phi_B}$  denotes a matrix constructed by the rows of the matrix  $M^{-1}F$  with the light flux density at the interface  $B$  removed. The elements of matrix  $M$  are

$$m_{ij} = \int_{\Omega_{dt}} D(\mathbf{r}) (\nabla \varphi_i(\mathbf{r})) \cdot (\nabla \varphi_j(\mathbf{r})) d\mathbf{r} + \int_{\Omega_{dt}} \mu_a(\mathbf{r}) \varphi_i(\mathbf{r}) \varphi_j(\mathbf{r}) d\mathbf{r} + \int_{\partial\Omega_{dt}} \varphi_i(\mathbf{r}) \varphi_j(\mathbf{r}) \frac{1}{\alpha(\mathbf{r})} d\mathbf{r}, \quad (9)$$

while the matrix  $F$  is defined as

$$f_{ij} = \int_{\Omega_{dt}} \varepsilon I(\mathbf{r}) \varphi_i(\mathbf{r}) \varphi_j(\mathbf{r}) \frac{1}{V(\mathbf{r})} d\mathbf{r}, \quad (10)$$

and matrix  $\Sigma$  is

$$\Sigma_{ij} = \int_R \int_B \frac{dB dR}{\pi \alpha(\mathbf{r}')} \varphi_i(\mathbf{r}') \varphi_j(\mathbf{r}_d) T(\mathbf{r}', \mathbf{r}_d). \quad (11)$$

Here,  $\varphi_i$  and  $\varphi_j$  are the nodal shape functions in the finite element discretization.

To reconstruct the concentration of phosphor nanoparticles, we construct the following  $l_1$ -norm-based regularization problem:

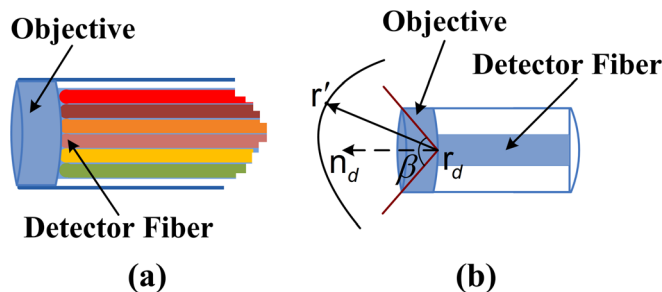


FIG. 2. Representative structure of the endoscopic probe. (a) Structure of the endoscopic probe used in medical endoscope, (b) definition of the aperture angle of the objective.

$$\hat{\rho} = \arg \min_{\rho > 0} \frac{1}{2} \left\| \Sigma [M^{-1}F]_{\phi_B} \rho - P \right\|_2^2 + \lambda |\rho|_1, \quad (12)$$

where  $\lambda$  is a regularization parameter. Equation (12) is the final formula and can be efficiently solved using a common optimization method, such as the primal-dual interior-point algorithm.<sup>10</sup>

## III. NUMERICAL SIMULATION AND PHANTOM EXPERIMENT

A tissue-mimicking-medium-based numerical simulation and a physical-phantom-based imaging experiment were performed to demonstrate the theoretical feasibility of the proposed eXLCT. To better evaluate the inverse reconstruction of eXLCT, we adopted some indicators, including the distance error (DiE), ratio between the interacted volume and total volume (IVTVR), and quantification error (QE). DiE is the distance between the maximal density position of the reconstructed source and the central location of the actual one, IVTVR is the ratio between the partial volume of the reconstructed source interacted with the actual one and the total volume of the reconstructed one, and QE is defined as the relative error between the reconstructed concentration and the actual one. For simplicity, the proposed eXLCT methodology is termed as the proposed method, and the eXLCT methodology which neglects the aperture angle is the original method.<sup>11</sup> It is worth noting that the aperture angle was set to be  $180^\circ$  in the reconstruction for the original method.

In the simulation, a cylindrical phantom with a radius of 100 mm and a height of 200 mm was used, which consisted of six objects to simulate the heterogeneity of biological tissues, being the geometrical parameters and the related optical properties detailed in Table I.<sup>11</sup> A spherical sub-region of 2 mm radius was centered at (0, -3, 0) mm and filled with phosphor nanoparticles with a concentration of  $1.5 \mu\text{g/ml}$ . The emission wavelength of the phosphor nanoparticles excited by X-rays was set to 802 nm according to the emission characteristics of  $\text{Gd}_2\text{O}_2\text{S}$  doped with thulium, and the NIR light yield  $\varepsilon$  was assumed to be  $0.15 \text{ cm}^3/\text{mg}$ . A cone X-ray beam with a micro focal diameter of  $100 \mu\text{m}$  operated at 50 kV and 30 mA perpendicularly irradiated the phantom. Simultaneously, a detector array of 5 mm radius was centered at (0, -30, 0) mm and longitudinally translated from the height of -2 to 2 mm along the z-axis direction, acquiring the emitted NIR light endoscopically. In the simulation, the aperture angle  $\beta$  was set to be  $120^\circ$  for the forward



TABLE I. Detailed geometrical parameters and related optical properties for simulations (in units of mm).

Tissues	Shape	Center	Size	$\mu_a$	$\mu'_s$
T <sub>1</sub>	Cylinder	(0, 0, 0)	(100, 100, 200)	0.0050	1.2273
T <sub>2</sub>	Ellipsoid	(−70, 0, 0)	(20, 50, 50)	0.2630	2.2091
T <sub>3</sub>	Ellipsoid	(0, −70, 0)	(50, 20, 20)	0.0881	2.3583
T <sub>4</sub>	Ellipsoid	(0, 20, 0)	(40, 30, 30)	0.0786	1.0066
T <sub>5</sub>	Ellipsoid	(0, −30, 0)	(25, 15, 15)	0	0
T <sub>6</sub>	Cylinder	(0, 75, 0)	(15, 15, 150)	0.1021	2.4144
T <sub>7</sub>	Ellipsoid	(70, 0, 0)	(20, 50, 50)	0.2630	2.2091

problem to obtain endoscopic measurements. Reconstructed results for both the proposed and original methods are shown in Figs. 3(a) and 3(b), respectively. Detailed comparisons are listed in Table II. From Fig. 3 and Table II, we find that the localization of the actual phosphor nanoparticles was well resolved on the reconstructed images for both methods, for which the same DiE was obtained and smaller than the radial size of the phosphor nanoparticles. However, from the IVTVR, we find that the number of reconstructed elements of the original method gathered at the actual region was slightly larger than that of the proposed method. On the other hand, a very good quantification result was obtained for the proposed method, where the reconstructed concentration is slightly underestimated and the QE is 4%. However, the reconstructed concentration was greatly overestimated for the original method, with a QE larger than 40%, mainly due to neglecting the aperture angle of the objective. Thus, we conclude that the aperture angle of the objective greatly affects the reconstructed concentration of phosphor nanoparticles and must be considered in the eXLCT approaches if quantification is needed.

In the imaging experiment, a cubic phantom made of nylon, with a side length of 30 mm, was used to illustrate the effectiveness of the eXLCT methodology. Two holes with

TABLE II. Detailed comparison of the reconstructed results for the simulation.

Simulation	DiE (mm)	IVTVR	Reconstructed concentration ( $\mu\text{g/ml}$ )	QE
Proposed method	3.94	0.77	1.44	4.00%
Original method	3.94	0.85	2.14	42.67%

different sizes were drilled in the phantom. One is drilled from the center of the top surface, with a diameter of 2 mm and a depth of 15 mm, which was used to jam in the europium (III) oxide ( $\text{Eu}_2\text{O}_3$ ) powder of 2 mm height (about 1 mg); the other is drilled from the center of the side surface, with a diameter of 10 mm and a depth of 12 mm, which was used to insert the endoscopic detector. The optical properties of the gray region in the phantom (shown in Fig. 4) were  $\mu_a = 0.0138 \text{ mm}^{-1}$  and  $\mu'_s = 0.91 \text{ mm}^{-1}$ , and those of the white region were set to be zero. The cone-beam X-rays from the X-ray tube with the target material of Tungsten scanned the phantom to stimulate the  $\text{Eu}_2\text{O}_3$  and obtain the structure of the phantom, operating at 50 kV and 1 mA. The luminescent light emitted from the  $\text{Eu}_2\text{O}_3$  was acquired by an endoscopic imaging system that organically integrates a bronchofibroscope with an aperture angle of  $90^\circ$  and a electron multiplying CCD (EMCCD) using an optical adapter. After the luminescent image was obtained, the distribution of the injected  $\text{Eu}_2\text{O}_3$  was reconstructed using both the proposed and original methods. The reconstructed result is shown in Fig. 4 and a detailed comparison is listed in Table III. From Fig. 4 and Table III, we find that both the proposed and original methods localized the distribution of the  $\text{Eu}_2\text{O}_3$ , with the same DiE of 1.94 mm, smaller than the size of the injected  $\text{Eu}_2\text{O}_3$ , and almost the same IVTVR. However, as illustrated in the numerical simulation, the reconstructed concentration of the original method was worse than that of the proposed method because of the overuse of the aperture

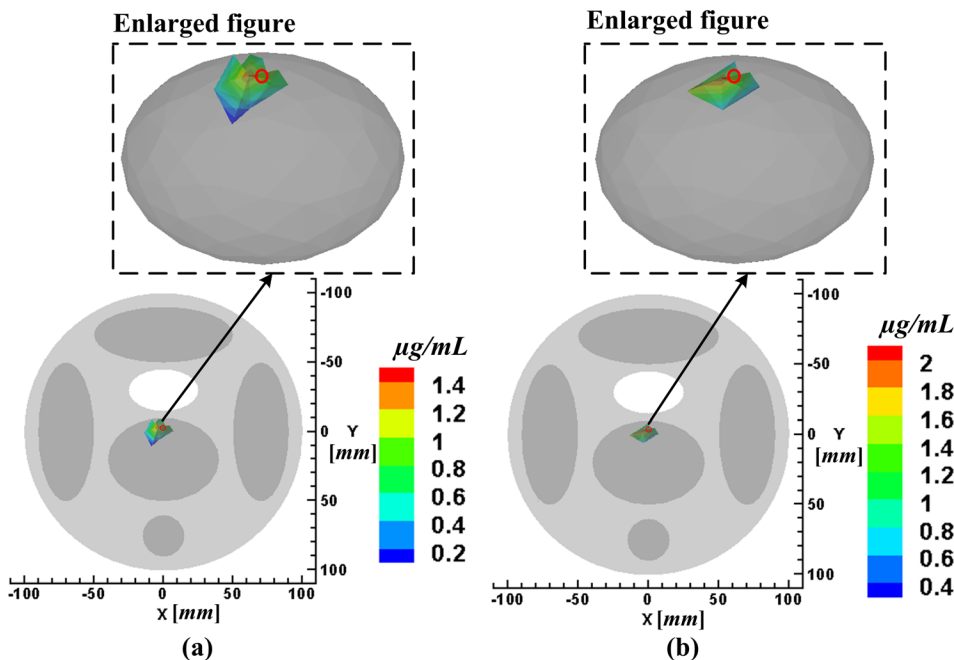


FIG. 3. Reconstructed distribution of the phosphor nanoparticles in the numerical simulation. (a) Result of the proposed eXLCT methodology, (b) result of the eXLCT methodology that neglects the aperture angle.

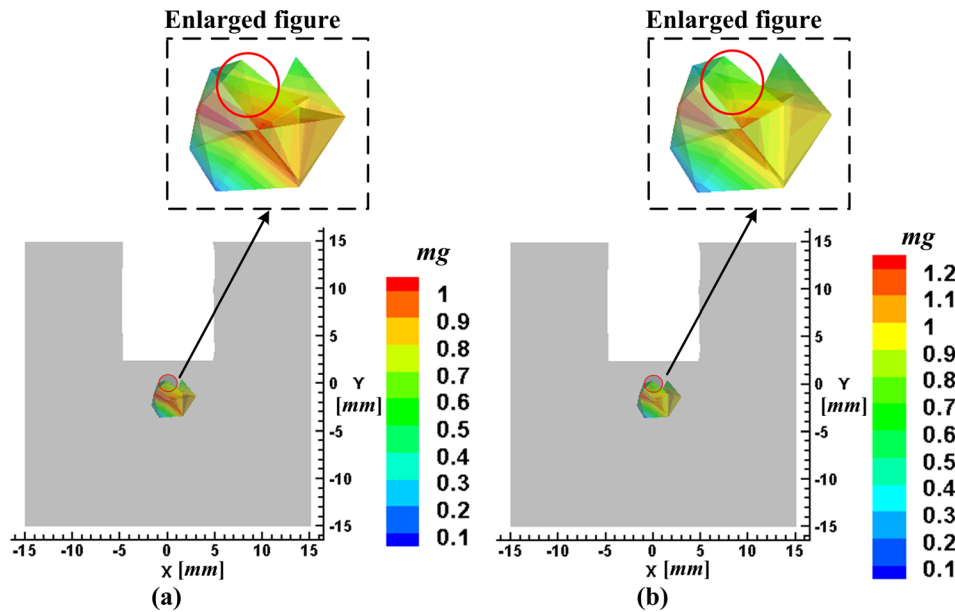


FIG. 4. Reconstructed distribution of the europium (III) oxide powder in the imaging experiment. (a) Result of the proposed eXLCT methodology, (b) result of the eXLCT methodology that neglects the aperture angle.

TABLE III. Detailed comparison of the reconstructed results for the imaging experiment.

Simulation	DiE (mm)	IVTVR	Reconstructed quantity (mg)	QE
Proposed method	1.94	0.5322	1.06	6%
Original method	1.94	0.5302	1.22	22%

angle. Reconstructed concentration of the proposed method was slightly overestimated with the QE of 6%. However, that of the original method was greatly overestimated with a QE larger than 20%. Furthermore, a better morphological distribution was obtained by the proposed method, as seen in the enlarged figure of Fig. 4. Additionally, from Fig. 4, we also find that the reconstructed elements for both methods did not approach the actual region ideally, although acceptable DiE and IVTVR were obtained. This is probably due to the insufficient measurements on the endoscopic probe, which increased the ill-posedness of the reconstruction problem. On all accounts, the proposed eXLCT methodology indeed exhibited its superiority, especially in the application of quantitative reconstruction.

#### IV. CONCLUSION

We have proposed a novel eXLCT methodology and validated its theoretical basis with a tissue-mimicking-medium-based numerical simulation and a physical-phantom-based imaging experiment. In the methodology, cone-beam X-rays were employed to irradiate the sample and obtain its anatomical structure, which overcomes the disadvantage of a long scanning time in existing XLCT technology and provides dual-modality images of luminescence tomography and computed tomography. Furthermore, a forward light transport model was established by integrating the aperture angle of the objective equipped in an endoscopic probe, providing more

accurate quantification results. We believe that this endoscopic imaging method will overcome the limitations of eFDOT in the imaging of internal organs that are deep in a large animal or human body and open possibilities of optical tomography to new molecular imaging applications. Further studies will focus on validating the theoretical basis using animal models.

#### ACKNOWLEDGMENTS

This work was supported in part by the Program of the National Basic Research and Development Program of China (973) under Grant No. 2011CB707702, the National Natural Science Foundation of China under Grant Nos. 81090272, 81227901, 81101083, 81201137, the Open Research Project under Grant 20120101 from SKLMCCS, and the Fundamental Research Funds for the Central Universities.

- <sup>1</sup>V. Ntziachristos, J. Ripoll, L. V. Wang, and R. Weissleder, *Nat. Biotechnol.* **23**, 313 (2005).
- <sup>2</sup>X. Zhang and C. Badea, *Opt. Express* **17**, 5125 (2009).
- <sup>3</sup>P. Fortin, C. Genevois, A. Koenig, E. Heinrich, I. Texier, and F. Couillaud, *J. Biomed. Opt.* **17**, 126004 (2012).
- <sup>4</sup>D. Piao, H. Xie, W. Zhang, J. S. Krasinski, G. Zhang, H. Dehghani, and B. W. Pogue, *Opt. Lett.* **31**, 2876 (2006).
- <sup>5</sup>H. Zhao, X. Zhou, Y. Fan, and F. Gao, *J. X-Ray Sci. Technol.* **19**, 57 (2011).
- <sup>6</sup>A. S. Montcuquet, L. Herve, F. Navarro, J. M. Dinten, and J. I. Mars, *IEEE Trans. Biomed. Eng.* **58**, 2554 (2011).
- <sup>7</sup>G. Pratz, C. M. Carpenter, C. Sun, and L. Xing, *IEEE Trans. Med. Imaging* **29**, 1992 (2010).
- <sup>8</sup>W. Cong, H. Shen, and G. Wang, *J. Biomed. Opt.* **16**, 066014 (2011).
- <sup>9</sup>J. Ripoll, R. B. Schulz, and V. Ntziachristos, *Phys. Rev. Lett.* **91**, 103901 (2003).
- <sup>10</sup>Q. Zhang, H. Zhao, D. Chen, X. Qu, X. Chen, X. He, W. Li, Z. Hu, J. Liu, J. Liang, and J. Tian, *Opt. Commun.* **284**, 5871 (2011).
- <sup>11</sup>X. Chen, J. Liang, H. Zhao, X. Qu, D. Chen, Q. Zhang, X. Gao, and J. Tian, *Appl. Phys. Lett.* **99**, 073702 (2011).